

Approaching the ultimate superconducting properties of (Ba,K)Fe₂As₂ by naturally formed low-angle grain boundary networks

Kazumasa Iida^{1,7,*}, Dongyi Qin², Chiara Tarantini³, Takafumi Hatano^{1,7}, Chao Wang⁴, Zimeng Guo^{5,7}, Hongy Gao⁴, Hikaru Saito^{6,7}, Satoshi Hata^{4,5,7}, Michio Naito^{2,7}, Akiyasu Yamamoto^{2,7}

¹ Department of Materials Physics, Nagoya University, Furo-cho, Nagoya 464-8603, Japan

² Department of Applied Physics, Tokyo University of Agriculture and Technology, Koganei, Tokyo 184-8588, Japan

³ Applied Superconductivity Center, National High Magnetic Field Laboratory, Florida State University, Tallahassee, United States of America

⁴ The Ultramicroscopy Research Center, Kyushu University, 744 Motooka, Nishi, Fukuoka 819-0395, Japan

⁵ Interdisciplinary Graduate School of Engineering Sciences, Kyushu University, Kasuga, Fukuoka 816-8580, Japan

⁶ Institute for Materials Chemistry and Engineering, Kyushu University, Kasuga, Fukuoka 816-8580, Japan

⁷ JST CREST, Kawaguchi, Saitama 332-0012, Japan

*Corresponding author. E-mail: iida@mp.pse.nagoya-u.ac.jp

KEY WORDS: iron-based superconductors, thin films, grain boundary, epitaxy

Abstract

The most effective way to enhance the dissipation-free supercurrent in presence of magnetic field for type II superconductors is the introduction of defects that acts as artificial pinning centres (APCs) for the vortices. For instance, the in-field critical current density of doped BaFe_2As_2 (Ba122), one of the most technologically important Fe-based superconductors, has been improved over the last decade by APCs created by ion-irradiation. The technique of ion-irradiation has been commonly implemented to determine the ultimate superconducting properties. However, this method is rather complicated and expensive. Here, we report on a surprisingly high critical current density and strong pinning efficiency close to the crystallographic c -axis for a K-doped Ba122 epitaxial thin film without APCs, achieving performance comparable to ion-irradiated K-doped Ba122 single crystals. Microstructural analysis reveals that the film is composed of columnar grains having width around 30–60 nm. The grains are rotated around the b - (or a -) axis by 1.5° and around the c -axis by -1° , resulting in the formation of low-angle grain boundary networks. This study demonstrates that the upper limit of in-field properties reached in ion-irradiated K-doped Ba122 is achievable by grain boundary engineering, which is a simple and industrially scalable manner.

Introduction

Significant progress on the growth of Fe-based superconductors (FBS) thin films has been achieved over the last decade. As a result, high quality, epitaxial thin films of the technologically important FBS [e.g. Fe(Se,Te), doped $AeFe_2As_2$ (Ae : alkaline earth elements) and doped $LnFeAsO$ (Ln : lanthanoid elements)] are realised on different kinds of single-crystalline substrates and technical substrates¹⁻⁵ except for (Ba,K)Fe₂As₂ (K-doped Ba122). Realisation of epitaxial K-doped Ba122 has been challenging due to the difficulty in controlling volatile potassium. We have recently succeeded in growing K-doped Ba122 epitaxial thin films on fluoride substrates⁶, which gives a great opportunity to investigate their electrical transport properties. Our preliminary study shows that grain boundaries (GBs) are present in K-doped Ba122 despite no sign of weak-link behaviours.

GB with a misorientation angle larger than critical angle $\theta_c \sim 9^\circ$ becomes a detrimental defect to the critical current for most FBS^{3, 7, 8}. On the other hand, GB having a small misorientation angle less than θ_c does not impede the supercurrent flow. Rather, dislocation arrays in low-angle GB (LAGB) contribute to the flux pinning^{3, 7, 8}, leading to improvements of the critical current properties of FBS thin films. Indeed, several studies have shown a proof-of-principle of this concept by growing P- and Co-doped Ba122 thin films on technical substrates with oxides buffer layers having a different in-plane spread prepared by ion beam assisted deposition (IBAD)^{9, 10}. In both compounds, the larger the texture spread of Ba122 within θ_c , the higher the critical current density J_c , typically a few MAcm⁻² at 4 K. Additionally, J_c for the applied field parallel to the crystallographic c -axis ($H \parallel c$) is similar to or even higher than that for $H \parallel ab$ ^{10, 11}. It was later demonstrated that enhanced pinning performance is due to LAGBs acting as flux pinning centres¹².

However, other well-known techniques such as irradiation with protons and heavy-ions produce either isotropic or anisotropic defects (i.e. artificial pinning centres, APCs) significantly enhanced J_c above the value obtained by the aforementioned GB engineering. For instance, SmFeAs(O,F) single crystal with columnar defects produced by heavy-ion irradiation exhibits a high self-field J_c of 18~20 MAcm⁻² at 5 K, which is about 9~10 times the J_c of the pristine sample¹³. Similarly, Ba_{0.6}K_{0.4}Fe₂As₂ single crystals with point defects created by 3 MeV proton irradiation shows a self-field J_c of 11 MAcm⁻² at 2 K, which is ~4.6 times the J_c of the pristine sample¹⁴. Quite recently, Ba_{0.6}K_{0.4}Fe₂As₂ single crystal irradiated by 320 MeV Au ions shows a very high self-field J_c of over 20 MAcm⁻² at 2 K¹⁵, corresponding to a 12% of $J_d \sim 166$ MAcm⁻²¹⁶.

Here, we report on a surprisingly high self-field J_c of 14.4 MAcm⁻² at 4 K and strong pinning efficiency close to the crystallographic c -axis for K-doped Ba122 epitaxial thin film with LAGB networks. The pinning force density F_p for $H \parallel c$ exceeds 200 GNm⁻³ at 4 K and above 6 T, which is at a level comparable to the K-doped Ba122 single crystal with Pb-ions irradiation¹⁷.

Materials and methods

Thin film growth

K-doped Ba122 thin films were grown on CaF₂(001) at 395°C, a slightly lower temperature than in our previous investigation, by a custom designed molecular beam epitaxy using solid sources of Fe, As, Ba and In-K alloy⁶. Here, we used In-K alloy rather than pure K because of the good controllability of K content in the film as well as for safety issue. CaF₂ substrate was fixed on the sample holder using a Ag paste to ensure good thermal conduction. Prior to deposition, the substrate was heated to 600°C, kept at this temperature for 15 min for thermal cleaning, and subsequently cooled to 395°C. The compositions of all fluxes except for As was monitored in situ by electron impact emission spectrometry (Ba and Fe) and atomic absorption spectrometry (K). The obtained real-time information was feedback to the personal computer that controls Proportional-Integral-Differential (PID) of the resistive heaters. The As flux was provided constantly during growth. Compared with our previous films, the growth parameters (i.e. deposition temperature and evaporation rate for each flux) have been fully optimised as evidenced in Supplementary fig. S1. Unlike our previous investigation, no impurity phases were observed. Additionally, the average full width at half maximum value of the 103 ϕ -scan is 1.1°, which is smaller than our previous film⁶.

Microstructural analysis by transmission electron microscopy

Cross-sectional samples were prepared by a focused ion beam. Scanning transmission electron microscopy observation was performed by a TEM (JEOL ARM-200F) operated at an acceleration voltage of 200 kV. TEM-based scanning precession electron diffraction (PED) analysis was performed by a TEM (Thermo Fisher Scientific Tecnai G2 F20 equipped with NanoMEGAS ASTAR system) operated at an acceleration voltage of 200 kV. Details of crystal orientation mapping based on PED are described in Ref. 18. In this PED analysis, the convergence semi-angle of the incident electron beam was 1 mrad, the precession angle was 0.55°. The crystal orientation at each measurement point was determined by matching the PED pattern with template patterns pre-generated from the crystal structural data of K-doped Ba122¹⁹ and CaF₂²⁰. β and γ are defined as the angles between [001]CaF₂ and [001]K-doped Ba122, and [100] (or [010]) CaF₂ and [100] (or [010]) K-doped Ba122, respectively. Note that β and γ values in this measurement include uncertainty of ~0.4°, which was estimated from the standard deviation of crystal orientation determination on the CaF₂ substrate.

Electrical transport measurements

A small bridge of 38 μm width and 1 mm length was fabricated by laser cutting. The sample was mounted on a rotator holder in maximum Lorentz force configuration. The angle θ is measured from the crystallographic *ab*-plane. Current – Voltage (*I*–*V*) characteristics were measured by a 4-probe method into a commercial physical property measurement system [(PPMS) Quantum

Design]. The upper critical fields H_{c2} were defined as 90% of the normal state resistivity. The irreversibility fields H_{irr} were defined as the intersection between the resistivity traces and the resistivity criterion of 10^{-5} m Ω cm. An electric field criterion of 1 μ V/cm is used to estimate J_c .

Magnetic measurements

Magnetisation measurements were performed on the rectangular-shaped sample using a superconducting quantum interference device magnetometer [SQUID VSM, (MPMS3) Quantum Design] using. The temperature dependence of susceptibility was measured with a magnetic field of 1 mT applied parallel to the *ab*-plane. Magnetic J_c was determined using the Bean model from the field dependence of magnetisation curves.

Results

Microstructure

As revealed by structural characterisation using X-ray diffraction, K-doped Ba122 was phase-pure and epitaxially grown on CaF₂(001) (Supplementary fig. S1). To evaluate the nanostructure of the grain boundaries, a cross section was observed by scanning transmission electron microscopy (STEM, fig. 1a) and analysed by TEM-based scanning precession electron diffraction (PED). The incident direction of the electron beam is approximately parallel to the [110] direction of the CaF₂(001) substrate. An annular dark-field (ADF) image in fig. 1a shows columnar grains growing in the *z* direction, which is more clearly seen in a virtual dark field image of 008 reflection (fig. 1b). The width of columnar grains is 30–60 nm. The epitaxial relationship is revealed as (001)[110]K-doped Ba122 || (001)[100]CaF₂ by the PED patterns (fig. 1c and d), which is consistent with the structural characterisation by X-ray diffraction (Supplementary fig. S1). Crystal rotations of K-doped Ba122 around the *b*-axis (equivalent to the *a*-axis) and the *c*-axis were calculated from the crystal orientation data separately and are plotted as two-dimensional maps in fig. 1e and f. For clarity, the crystal rotation angles β (around the *b*- and *a*-axis) and γ (around the *c*-axis) with respect to CaF₂ are shown in fig. 1g and h. As clearly seen in the line profiles (fig. 1i), the average grain rotation around the *b*- (or *a*-) axis is $\Delta\beta_{\text{average}} = 1.5^\circ$ and around the *c*-axis is $\Delta\gamma_{\text{average}} = -1^\circ$ with respect to the ideal values (i.e. $\Delta\beta = \beta - \beta_{\text{ideal}}$, where β_{ideal} is 0° , and $\Delta\gamma = \gamma - \gamma_{\text{ideal}}$, where γ_{ideal} is 45°), resulting in the formation of LAGB networks. As can be seen in Supplementary fig. S2, the [001] of K-doped Ba122 was tilted toward the [0 $\bar{1}$ 0] in our coordinate system. The distribution of β over the 2880 points shows that a large fraction locates between 0° – 3.5° with a peak of 1.5° (Supplementary fig. S2). For completeness, the distribution of γ is also shown in Supplementary fig. S3. This fact reflects the results of angular dependent of J_c measurements, which will be discussed later.

Resistivity measurements

$T_{c,90}$, defined as 90% of normal state resistivity, of our K-doped Ba-122 thin film is 35.2 K

(Supplementary fig. S4). The zero-resistivity temperature $T_{c,0}$ is 33 K, corresponding to the onset temperature of the diamagnetic signal measured by the temperature dependence of susceptibility. Therefore, the transition width, defined as $T_{c,90} - T_{c,0}$ is 2.2 K.

To determine the upper critical field H_{c2} and the irreversibility field H_{irr} , the temperature dependence of resistivity was measured in field up to 16 T (fig. 2a and b). As increasing applied magnetic fields, a clear shift of T_c to lower temperatures together with a broadening of the superconducting transition is observed for both main crystallographic orientations. The broadening of the transition is more obvious for $H \parallel c$ than $H \parallel ab$, however, such broadening is not so significant compared with $LnFeAsO$ ²¹ due to the weak thermal fluctuation. It is also worth mentioning that the foot structure in the vicinity of zero resistance arising from the presence of high angle GBs, previously observed in Ref. 22, is not present here. Such foot structure is also due to the poor connectivity. Temperature dependence of the upper critical field H_{c2} and the irreversibility field H_{irr} are summarized in fig. 2c. The slopes of H_{c2} in the field range $0 \leq \mu_0 H \leq 2$ T are -20.1 TK^{-1} and -11.5 TK^{-1} for $H \parallel ab$ and $\parallel c$, respectively. Those values are much higher than the counterpart of single crystal²³. Another feature is that the slope of H_{irr} -line for $H \parallel c$ changes at around 2 T (inset of fig. 2c), which is reminiscent of $REBa_2Cu_3O_7$ (RE : rare earth elements, $REBCO$) thin films with the c -axis correlated defects²⁴. To identify the matching field, $\mu_0 H_{irr}$ is plotted as a function $1 - T/T_{irr}$, where T_{irr} is the irreversibility temperature (fig. 2d). As can be seen, the slope of the $\mu_0 H_{irr}$ -line changes from 1.77 to 1.02 at 2 T.

Pinning potential

To obtain the activation energy U_0 for vortex motion at given fields, linear fits of the Arrhenius plots for the resistivity curves are conducted (figs. 3a and b). Based on the thermally activated flux-flow model²⁵, the slope of linear fits corresponds to $-U_0$. In fact, on the assumption of the linear temperature dependence, $U(T,H)=U_0(H)(1-T/T_c)$, the following two formulae, $\ln \rho(T,H)=\ln \rho_0(H)-U_0(H)/T$ and $\ln \rho_0(H)=\ln \rho_{0f}+U_0(H)/T_c$, (derived from $\rho(T,H)=\rho_{0f} \exp[-U(T,H)/T]=\rho_{0f} \exp[-U_0(H)(1-T/T_c)/T]$) are obtained with ρ_{0f} being the pre-factor. As can be seen in fig. 3c, the activation energy U_0 for both $H \parallel c$ and $\parallel ab$ shows the same power law relation H^α in low fields up to 2 T: the exponent α is $\sim 0.05-0.07$, which indicates that the single vortex pinning prevails. In this regime, U_0 for both directions are 12000~13000 K, whereas the respective values of the $Ba_{0.72}K_{0.28}Fe_2As_2$ single crystal with $T_c=32$ K (i.e. underdoped sample) for $H \parallel ab$ and $\parallel c$ at 1 T are 8500 K and 5000 K²⁶. Above 2 T, for $H \parallel ab$, $\alpha \sim 0.5$ is consistent with a plastic pinning regime²⁷. On the other hand, for $H \parallel c$, α is 0.68, which is located between 0.5 and 1, where the exponent $\alpha=1$ is the theoretical prediction for collective pinning²⁸. It is interesting to note that for high field regime (i.e. 13~16 T) U_0 of our film is comparable to the single crystals²⁶.

The relationship between $\ln[\rho_0]$ and U_0 for both orientations is shown in fig. 3d, where the slope of linear fits corresponds to $1/T_c$. The respective T_c for $H \parallel c$ and $\parallel ab$ are 35.4 K and 35.5

K, which is close to $T_{c,90}$. This perfect scaling justifies the initial assumption of $U(T, H) = U_0(H)(1 - T/T_c)$ in a wide range of temperatures.

Field dependence of J_c obtained from the transport and magnetisation measurements

Figure 4a shows the in-field J_c properties for the K-doped Ba122 thin film measured by the $I-V$ (or current density J – electric field E) characteristics at various temperatures. $E-J$ curves for $H \parallel c$ are shown in Supplementary fig. S5. At 30 K for both $H \parallel c$ and $\parallel ab$, J_c gradually decreases with increasing fields. However, below 25 K J_c is almost insensitive against applied magnetic fields and a high J_c above $2 \times 10^5 \text{ A cm}^{-2}$ is maintained on the entire investigated field range. The most striking feature is that J_c for $H \parallel c$ is exceeding that for $H \parallel ab$ with decreasing temperature, opposite to the expected intrinsic behaviour related to the anisotropy of H_{c2} . Similar features with inverse anisotropy caused by strong c -axis correlated defects were observed before, for instance in Co-doped Ba122²⁹ and REBCO^{24, 30, 31}. These results infer that the strong c -axis pinning is active at $T \leq 25 \text{ K}$. It is worth mentioning that J_c peak for $H \parallel c$ is prominent at high temperatures for REBCO but it strongly suppresses with decreasing temperature³², which is different from FBS.

To prevent overheating of the contact leads/pads and possible sample damage, the $E-J$ characterisation was limited at low fields and temperatures. Hence, for completeness, the field dependence of magnetisation to extract J_c was measured on a rectangular sample cut from the same film used for transport measurements on a wider temperature range (Supplementary fig. S6). J_c calculated from the Bean model is shown in fig. 4b. Except for 28 K, J_c has a weak field dependence, which is consistent with the transport J_c . At 4 K, self-field J_c reaches 14.4 MAcm^{-2} , corresponding to a $\sim 9\%$ of the depairing current density J_d ¹⁶. Temperature dependence of J_c measured by electrical transport measurements follow well the magnetization J_c (fig. 4c), although the electric field criterion E_c of the former is higher than the latter. The data at 30 K slightly deviating from the trend is likely due to the fluctuations close to the T_c .

The field dependence of F_p calculated from fig. 4a is summarised in fig. 4d. Because of the presence of strong c -axis pinning at $T \leq 25 \text{ K}$, the maximum F_p is always recorded for $H \parallel c$ within our experimental condition (i.e. up to 16 T).

Angle dependence of J_c obtained from the transport measurement

To get better understanding of the pinning efficiency, measurements of the angular dependences of J_c were conducted at various temperatures and field strength (fig. 5). For all fields, J_c peaks around $H \parallel c$ ($\theta = 90^\circ$) are weak at 30 K, however, they become intense at $T \leq 25 \text{ K}$. The peak position of J_c around $H \parallel c$ is away from the c -axis by $\sim 4^\circ$, indicating that “the correlated defects” are slightly tilted. This is because the columnar grains of K-doped Ba122, which creates LAGBs along the grains, grew unidirectionally at an incline of a few degrees with respect to the substrate normal. To clearly see the effect of correlated defects on J_c , J_c anisotropy defined as J_c/J_c^{ab} , where J_c^{ab} is J_c at $\theta = 180^\circ$, is plotted at the fixed magnetic field (fig. 5e-g). The black dashed lines are

positioned at 94° to clearly see the J_c peaks. At 4 T and 30 K, J_c/J_c^{ab} is about 0.5 for $H \parallel c$ (fig. 5e), increasing to ~ 1.6 at low temperatures. This is a clear indication that the strong pinning around $H \parallel c$ is activated between 30 and 25 K. As increasing applied magnetic fields, a full evolution of the angular dependence of J_c/J_c^{ab} can be observed from a roughly regular behaviour with maximum at 180° for $H \parallel ab$ (e.g. 16 T and 25 K) to an almost isotropic one (e.g. 10 T and 25 K as well as 16 T and 20 K), and finally to a behaviour strongly affected by c -axis correlated pinning at the lowest temperatures.

Discussions

Through microstructural analyses and electrical transport measurements, “ c -axis correlated defect” in our K-doped Ba122 thin film is identified as low angle grain boundary (LAGB). On the assumption that the mean distance d of correlated pinning is identical to that of the width of K-doped Ba122 grains (i.e. 30–60 nm), the matching field $B_\phi \sim \phi_0/d^2$ is around 2 T at which a kink of H_{irr} is observed (fig. 2c and d, ϕ_0 being the flux quantum). As shown in fig. 5, this pinning is strongly temperature dependent, which is due presumably to the crossover between the in-plane coherence length of K-doped Ba122 and the defect size. The correlated GBs pinning and networks improve not only self-field J_c but also in-field J_c for H close to the c -axis. Consequently, the anisotropy of J_c is inverted with respect to H_{c2} . A similar observation was reported in Ref. 33, where the GBs between columnar grains in MgB₂ thin films grown by e-beam evaporation worked as pinning centres.

The tilted growth of K-doped Ba122 is due presumably to the geometrical configuration of the deposition sources together with the deposition without rotating substrates. In our setup, vapour flux arrives at the substrate with an oblique angle. Additionally, adatoms are expected to diffuse relatively slow on the substrate, since the substrate temperature was low compared with the melting temperature of K-doped Ba122 (832°C)³⁴. Hence, the shadowing effect³⁵, which limits the formation of new nuclei during the deposition behind initially formed-nuclei, is pronounced, resulting in the inclined columnar growth.

A pinning force density F_p of 114 GNm⁻³ is recorded even at 15 K and 14–16 T (obtained from the transport measurement) and exceeds 200 GNm⁻³ at 4 K and field above 6 T (the data at 4 K is obtained from the magnetisation measurements in fig. 4b). In fig. 6, the field dependence of F_p for our K-doped Ba122 thin film is plotted. For comparison, we also plotted the following data of pinning enhanced Ba122 single crystals and thin films with different dopants: K-doped Ba122 single crystals with Pb-ions irradiation measured at 5 K¹⁷, Co-doped Ba122 thin film with large amounts of stacking faults measured at 4.2 K³⁵, Co-doped Ba122 thin film with 3mol% BaZrO₃ (BZO) measured at 5 K³⁶, and P-doped Ba122 with 3mol% BZO measured at 4.2 K and 15 K³⁷. As can be seen, up to 4 T, F_p of our K-doped Ba122 thin film is the highest among the pinning enhanced Ba122. Albeit the F_p data above 7 T are missing, the extrapolated value at 9 T for the

K-doped Ba122 thin film is comparable to the highest value reported for Co-doped Ba122 thin film.

Huge improvement of the superconducting properties of our K-doped Ba122 thin film without APCs is due to a high density of correlated pinning centres created by LAGB networks. Unlike Co- and P-doped Ba122 thin films, the growth temperature of K-doped Ba122 thin films is quite low ($\sim 400^\circ\text{C}$). This low temperature synthesis may lead to small grain size, and hence, the increase of the density of LAGB. It is worth mentioning that the dislocation density increases with increasing the grain boundary angle. Hence, further improvement of in-field J_c is possible by enlarging the texture spread within the critical angle θ_c . Grain boundary engineering present in this study highlights the possible novel approach to improve the superconducting properties, which is a simple and industrially scalable manner.

Conclusion

Herein, we have investigated nanoscale microstructure of K-doped Ba122 epitaxial thin film grown on CaF_2 by molecular beam epitaxy. The nanoscale crystal orientation mapping shows that the film is composed of columnar grains having width around 30–60 nm. The average grain rotation around the b - (or a -) axis is 1.5° and around the c -axis is -1° with respect to the ideal values, resulting in the formation of low-angle grain boundary networks. Thanks to LAGB networks, superior superconducting properties of K-doped Ba122 are realised: the pinning force density F_p for $H \parallel c$ exceeds over 200 GNm^{-3} at 4 K and above 6 T, which is comparable to the best performing K-doped Ba122 by ion-irradiation.

References

1. Hiramatsu, H., Katase, T., Kamiya, T. & Hosono, H. Thin Film Growth and Device Fabrication of Iron-Based Superconductors. *J. Phys. Soc. Jpn.* **81**, 011011 (2012).
2. Li, Q., Si, W. & Dimitrov, I. K. Films of iron chalcogenide superconductors. *Rep. Prog. Phys.* **74**, 124510 (2011).
3. Iida, K., Hänisch, J. & Tarantini, C. Fe-based superconducting thin films on metallic substrates: Growth, characteristics, and relevant properties. *Appl. Phys. Rev.* **5**, 031304 (2018).
4. Sakoda, M., Iida, K. & Naito, M. Recent progress in thin film growth of Fe-based superconductors: superior superconductivity achieved by thin films. *Supercond. Sci. Technol.* **31**, 093001 (2018).
5. Hänisch, J., Iida, K., Hühne, R. & Tarantini, C. Fe-based superconducting thin films-preparation and tuning of superconducting properties. *Supercond. Sci. Technol.* **32**, 093001 (2019).
6. Qin, D. et al. A. Realization of epitaxial thin films of the superconductor K-doped BaFe_2As_2 .

- Phys. Rev. Materials* **5**, 014801 (2021).
7. Iida, K., Hänisch, J. & Yamamoto, A. Grain boundary characteristics of Fe-based superconductors. *Supercond. Sci. Technol.* **33**, 043001 (2020).
 8. Hänisch, J. & Iida, K. Superconductivity From Materials Science to Practical Applications (Berlin: Springer) pp 269-302, ch 10 (2020).
 9. Katase, T. et al. Biaxially textured cobalt-doped BaFe₂As₂ films with high critical current density over 1 MA/cm² on MgO-buffered metal-tape flexible substrates. *Appl. Phys. Lett.* **98**, 242510 (2011).
 10. Sato, H., Hiramatsu, H., Kamiya, T. & Hosono, H. Enhanced critical-current in P-doped BaFe₂As₂ thin films on metal substrates arising from poorly aligned grain boundaries. *Sci. Rep.* **6**, 36828 (2016).
 11. Xu, Z., Yuan, P., Fan, F., Chen, Y. & Ma, Y. Transport properties and pinning analysis for Co-doped BaFe₂As₂ thin films on metal tapes. *Supercond. Sci. Technol.* **31**, 055001 (2018).
 12. Iida, K. et al. High-field transport properties of a P-doped BaFe₂As₂ film on technical substrate. *Sci. Rep.* **7**, 39951 (2017).
 13. Fang, L. et al. Huge critical current density and tailored superconducting anisotropy in SmFeAsO_{0.8}F_{0.15} by low-density columnar-defect incorporation. *Nat. Commun.* **4**, 2655 (2013).
 14. Taen, T., Ohtake, F., Pyon, S., Tamegai, T & Kitamura, H. Critical current density and vortex dynamics in pristine and proton-irradiated Ba_{0.6}K_{0.4}Fe₂As₂. *Supercond. Sci. Technol.* **28**, 085003 (2015).
 15. Takahashi, A. et al. Effects of Splyaed Columnar Defects on Critical Current Density in CaKFe₄As₄. *J. Phys.: Conf. Ser.* **1590**, 012015 (2020).
 16. Mishev, V., Nakajima, M., Eisaki, H. & Eisterer, M. Effects of introducing isotropic artificial defects on the superconducting properties of differently doped Ba-122 based single crystals. *Sci. Rep.* **6**, 27783 (2015).
 17. Fang, L. et al. High, magnetic field independent critical currents in (Ba,K)Fe₂As₂ crystals. *Appl. Phys. Lett.* **101**, 012601 (2012).
 18. Rauch, E. F. et al. Automated nanocrystal orientation and phase mapping in the transmission electron microscope on the basis of precession electron diffraction. *Z. Kristallogr.* **225**, 103–109 (2010).
 19. Zaikina, J. V. et al. Facile Synthesis of Ba_{1-x}K_xFe₂As₂ Superconductors via Hydride Route. *J. Am. Chem. Soc.* **136**, 16932–16939 (2014).
 20. Cheetham, A. K., Fender, B. E. F. & Cooper, M. J. Defect structure of calcium fluoride containing excess anions I. Bragg scattering. *J. Phys. C* **4**, 3107–3121 (1971).
 21. Jaroszynski, J., Hunte, F., Balicas, L., Jo, Y-j., Raicevic, I., Gurevich, A. & Larbalestier, D.

- C. Upper critical fields and thermally-activated transport NdFeAsO_{0.7}Fe_{0.3} single crystal. *Phys. Rev. B* **78**, 174523 (2008).
22. Lee, N., Jung, S-G., Kim, D. & Kang, W. Potassium-doped BaFe₂As₂ superconducting thin films with a transition temperature of 40 K. *Appl. Phys. Lett.* **96**, 202505 (2010).
 23. Ishida, S. et al. Doping-dependent critical current properties in K, Co, and P-doped BaFe₂As₂ single crystals. *Phys. Rev. B* **95**, 014517 (2017).
 24. Horide, T. et al. Influence of matching field on critical current density and irreversibility temperature in YBa₂Cu₃O₇ films with BaMO₃ (M=Zr, Sn, Hf) nanorods. *Appl. Phys. Lett.* **108**, 082601 (2016).
 25. Palstra, T. T. M., Batlogg, B., Schneemeyer, L. F. & Waszczak, J. V. Thermally Activated Dissipation in Bi_{2.2}Sr₂Ca_{0.8}Cu₂O_{8+δ}. *Phys. Rev. Lett.* **61**, 1662-1665 (1989).
 26. Wang, X-L. et al. Very strong intrinsic flux pinning and vortex avalanches in (Ba,K)Fe₂As₂ superconducting single crystals. *Phys. Rev. B* **82**, 024525 (2010).
 27. Geshkenbein, V., Larkin, A., Feigl'man, M. & Vinokur, V. Flux pinning and creep in high-*T_c* superconductors. *Physica C* **162-164**, 239-240 (1989).
 28. Blatter, G., Feigl'mann, M. V., Geshkenbin, V. B., Larkin, A. I. & Vinokur, V. M. Vortices in high-temperature superconductors. *Rev. Mod. Phys.* **66**, 1125-1388 (1994).
 29. Tarantini, C. et al. Strong vortex pinning in Co-doped BaFe₂As₂ single crystal thin films. *Appl. Phys. Lett.* **96**, 142510 (2010).
 30. Matsui, H. et al. 4-fold enhancement in the critical current density of YBa₂Cu₃O₇ films by practical ion irradiation. *Appl. Phys. Lett.* **101**, 232601 (2012).
 31. Opherden, L. et al. Large pinning forces and matching effects in YBa₂Cu₃O_{7-δ} thin films with Ba₂Y(Nb/Ta)O₆ nano-precipitates. *Sci. Rep.* **6**, 21188 (2016).
 32. Xu, A. et al. Broad temperature pinning study of 15 mol.% Zr-added (Gd,Y)-Ba-Cu-O MOCVD coated conductors. *IEEE. Trans. Appl. Supercond.* **25**, 6603105 (2015).
 33. Kitaguchi, H. et al. MgB₂ films with very high critical current densities due to the strong grain boundary pinning. *Appl. Phys. Lett.* **85**, 2842-2844 (2004).
 34. Peng, J. B., Sun, G. L. & Lin, C. T. Investigation of thermal behavior and crystal growth of iron pnictides using Sn flux. *J. Cryst. Growth* **316**, 85-89 (2011).
 35. Dirks, A. G. & Jeamy, H. J. Columnar microstructure in vapor-deposited thin films. *Thin Solid Films* **47**, 219-233 (1977).
 36. Yuan, P. et al. Vortex pinning properties in Co-doped BaFe₂As₂ thin films with a high critical current density over 2 MA cm⁻² at 9 T. *Supercond. Sci. Technol.* **30**, 025001 (2016).
 37. Lee, J. et al. High critical current density over 1 MAcm⁻² at 13 T in BaZrO₃ incorporated Ba(Fe,Co)₂As₂ thin film. *Supercond. Sci. Technol.* **30**, 085006 (2017).
 38. Miura, M. et al. Enhanced critical current density in BaFe₂(As_{0.66}P_{0.33})₂ nanocomposite

superconducting films. *Supercond. Sci. Technol.* **32**, 064005 (2019).

Acknowledgements

We thank Wai-Kwong Kwok (Argonne National Laboratory) for data¹⁷, Yanwei Ma (Chinese Academy of Science) for data³⁶, Jongmin Lee and Sanghan Lee (Gwangju Institute of Science and Technology) for data³⁷, and Masashi Miura (Seikei University) for data³⁸. This work was supported by JST CREST Grant Number JPMJCR18J4. A portion of work was performed at the National High Magnetic Field Laboratory, which was supported by National Science Foundation Cooperative Agreement No. DMR-1644779 and the State of Florida. It was also supported by US Department of Energy Office of High Energy Physics under the grant number DE-SC0018750. This work was also partly supported by Advanced Characterization Platform of the Nanotechnology Platform Japan sponsored by the Ministry of Education, Culture, Sports, Science and Technology (MEXT), Japan.

Author Contributions

K.I. and A.Y. designed the study. K.I. and C.T. wrote manuscript together with D.Q., H.S., S.H., M.N. and A.Y.. Thin films preparation, structural characterisations by XRD, and micro bridge fabrications were carried out by D.Q., M.N, K.I., T.H. and C.T.. Microstrutural characterisations by TEM were performed by C.W., Z.G., H.G., H.S. and S.H., and C.T. conducted in-field electrical transport measurements.

Conflict of Interests

The authors declare that they have no conflict of interest.

Figures captions

Figure 1 | Microstructural analyses by TEM. **a**, Cross-sectional view obtained by ADF-STEM. **b**, Virtual dark field image of 008 reflection of K-doped Ba122. **c**, Typical PED patterns extracted from the K-doped Ba122 thin film (red cross in **b**) and **d**, the CaF₂ substrate (green cross in **b**). **e**, β rotation map and **f**, γ rotation map obtained from the K-doped Ba122 thin film. The z -axis shows the distance from the interface between K-doped Ba122 and CaF₂, the same direction as shown in **a**. The ideal angles, 0° and 45°, are defined as light-green and red colour in **e** and **f**, respectively. **g**, Schematic illustration the crystal rotation angles β (around the [100]-axis) and **h**, γ (around [001]-axis) with respect to CaF₂ as the reference. **i**, Line profiles of β rotation and γ rotation extracted along the black broken lines in **e** and **f**, respectively. The lines of $\beta = 0^\circ$ and $\gamma = 45^\circ$ are marked for comparison.

Figure 2 | In-field resistivity measurements and the magnetic phase diagram for the K-doped Ba122 thin film. **a**, Resistivity curves for H parallel to the crystallographic c -axis and **b**, $H \parallel ab$ -plane. Field increment was 2 T from 2 to 16 T. Below 2 T, measurements were conducted at 0, 0.5, 1, and 2 T. **c**, Both H_{c2} and H_{irr} are plotted as a function of temperature. The solid symbols represent H_{c2} and the open symbols show H_{irr} , respectively. For $H \parallel c$, the slope of H_{irr} changes around 2 T as indicated by the arrow. **d**, Logarithmic presentation of H_{irr} vs $1-T/T_{irr}$, where T_{irr} is the irreversibility temperature at self-field. The slope changes at 2 T, corresponding to the matching field.

Figure 3 | Arrhenius plots of the resistivity curves shown in figs. 2a and b, and the resultants pinning potential U_0 and prefactor ρ_0 for the K-doped Ba122 thin film. **a**, For H parallel to the crystallographic c -axis and **b**, ab -plane. **c**, Field dependence of the pinning potential $U_0(H)$ for both main crystallographic orientations. **d**, $U_0(H)$ dependent of $\ln[\rho_0$ (m Ω cm)] for $H \parallel c$ and $\parallel ab$.

Figure 4 | Field dependence of the critical current density J_c measured by the transport and magnetisation methods. **a**, J_c - H characteristics for both main orientations obtained from the transport measurements. The solid symbols represent $H \parallel c$ and the open symbols show $H \parallel ab$, respectively. **b**, Field dependence of J_c evaluated from the magnetisation measurements using the extended Bean model. **c**, Temperature dependence of J_c for several applied fields $H \parallel c$. **d**, Field dependence of F_p calculated from **a**.

Figure 5 | Angular dependence of transport J_c for the K-doped Ba122 thin film. Measurement temperature was **a**, 30 K, **b**, 25 K, **c**, 20 K, and **d**, 15 K. At angles of $\theta=90^\circ$ and

180° correspond to $H \parallel c$ and $\parallel ab$, respectively. Angle dependence of J_c normalised by J_c for $H \parallel ab$ (J_c^{ab}) measured at **e**, 4 T, **f**, 10 T, and **g**, 16 T, respectively. The dashed lines are located at $\theta=94^\circ$ to clearly see the J_c peaks.

Figure 6 | Field dependence of the pinning force density F_p for $H \parallel c$. The F_p for K-doped Ba122 thin film measured at 4 K and 15 K. The respective F_p at 4 K and 15 K are calculated using the J_c - H data obtained from the magnetic and transport measurements. For comparison, the data of K-doped Ba122 single crystal with Pb-ions irradiation measured at 5 K¹⁷, Co-doped Ba122 thin film with a large amount of stacking faults measured at 4.2 K³⁶, Co-doped Ba122 thin film with 3 mol% BaZrO₃ (BZO) measured at 4.2 K³⁷, and P-doped Ba122 thin film with 3mol% BZO measured at 4 K and 15 K³⁸ are also plotted.

Figure 2

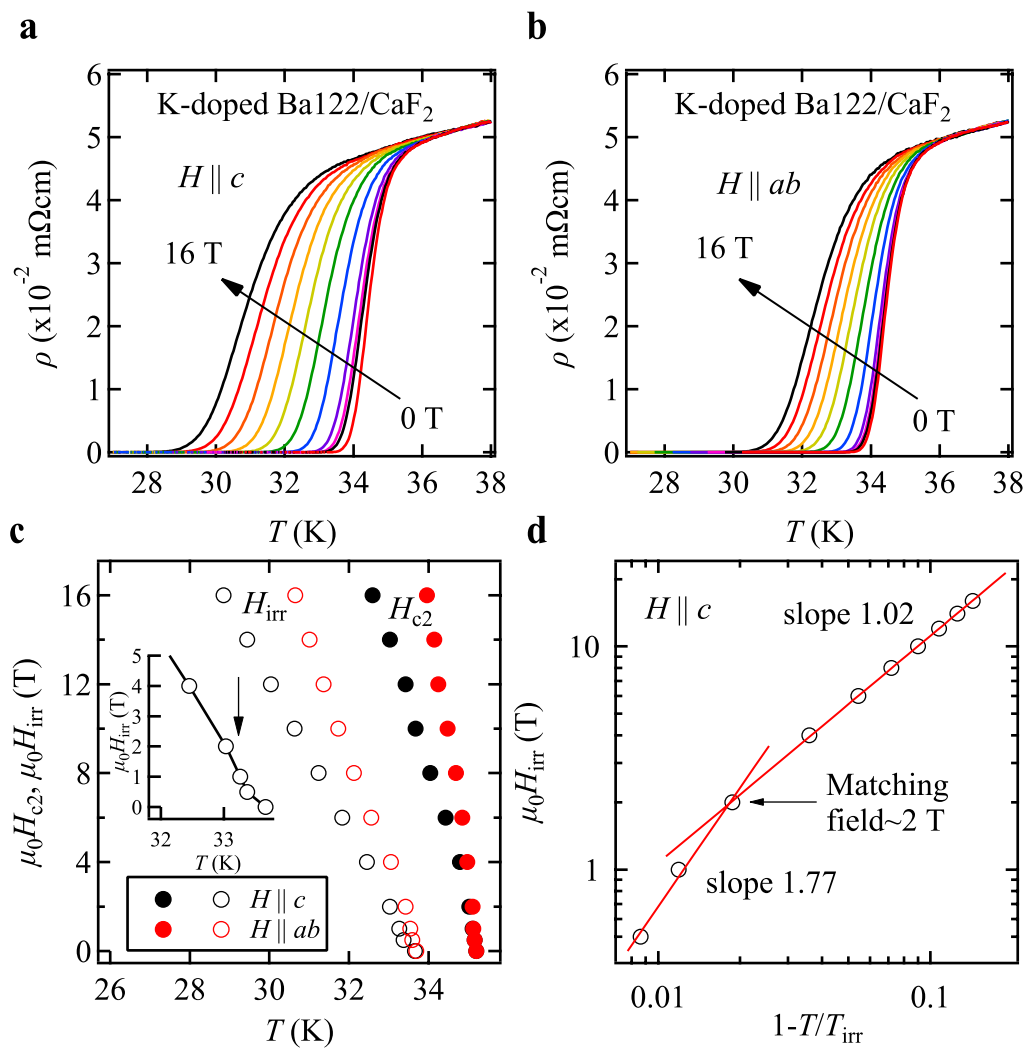


Figure 3

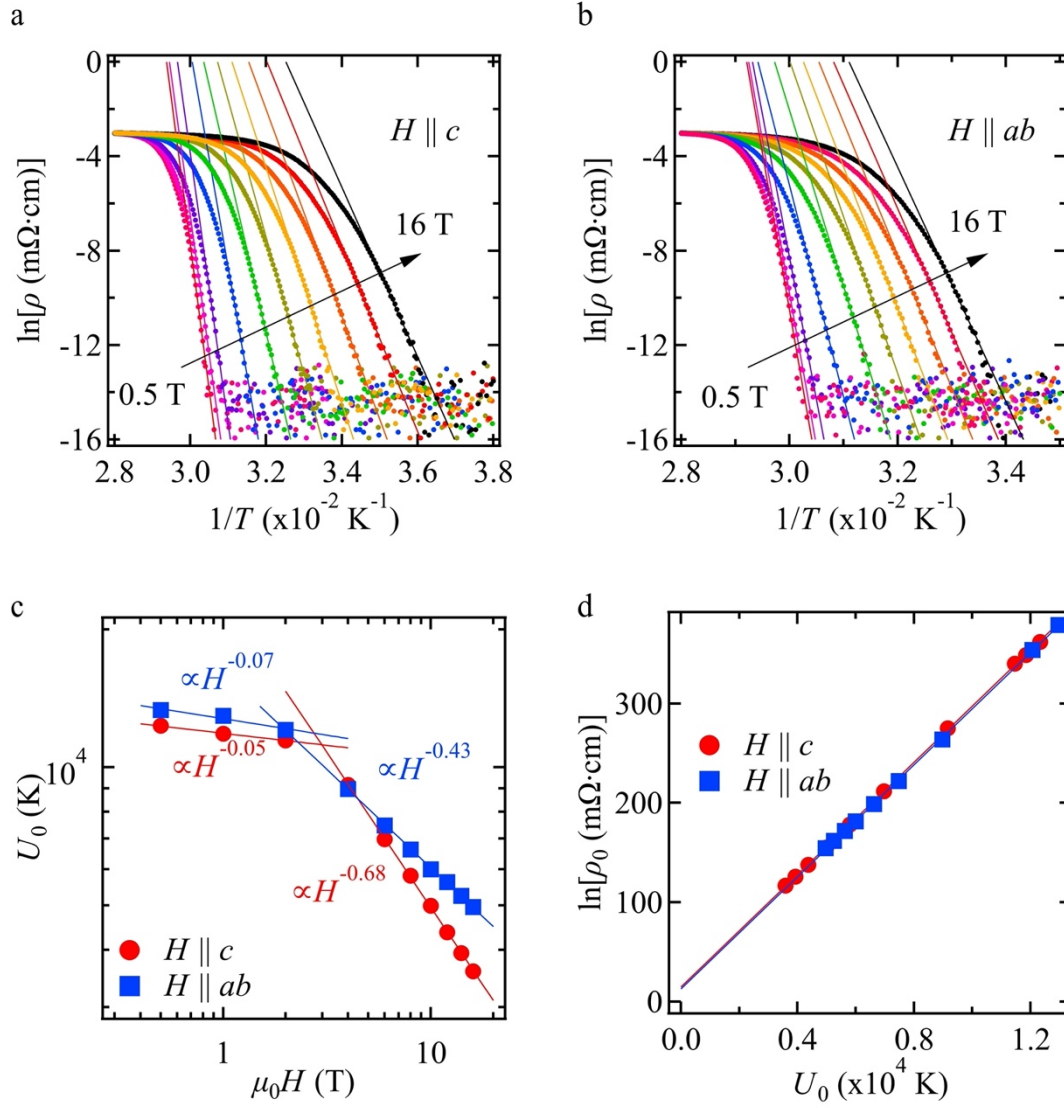


Figure 4

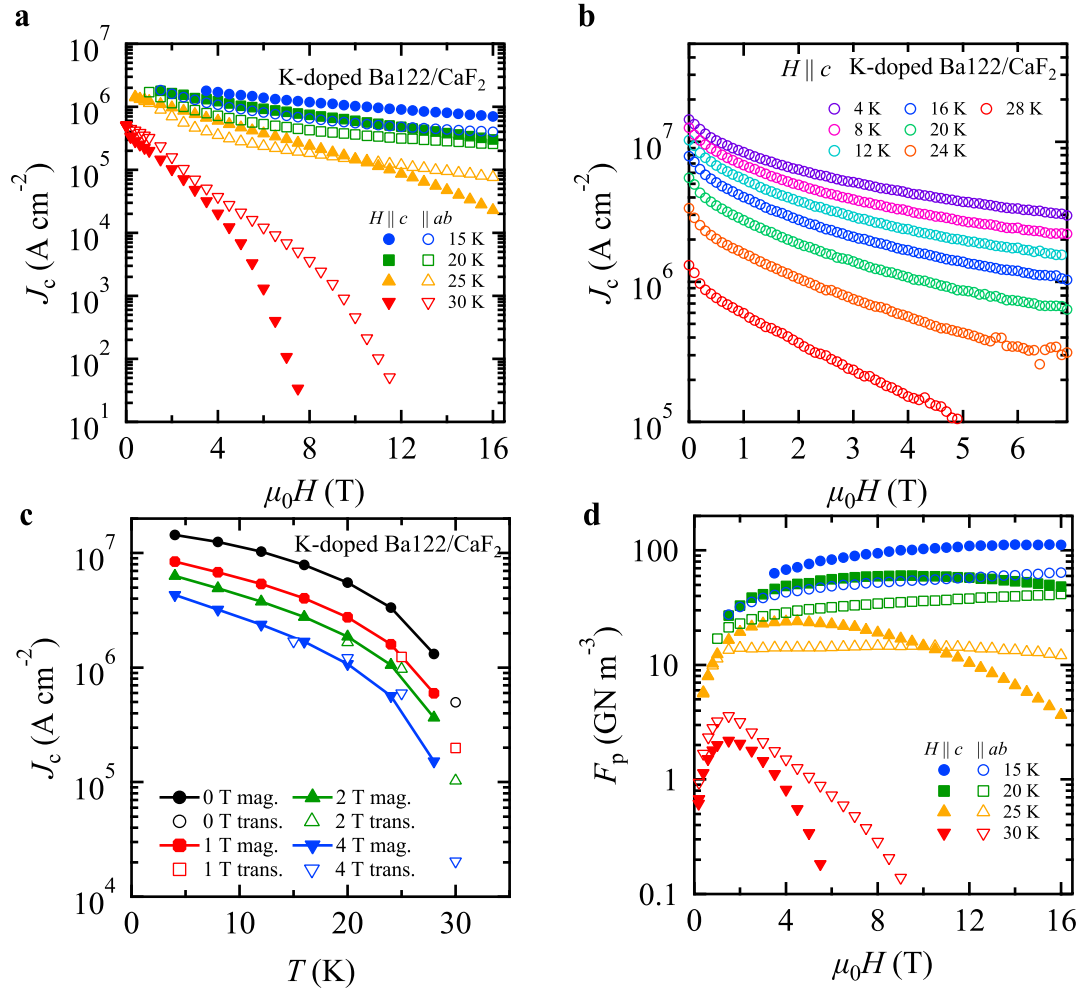


Figure 5

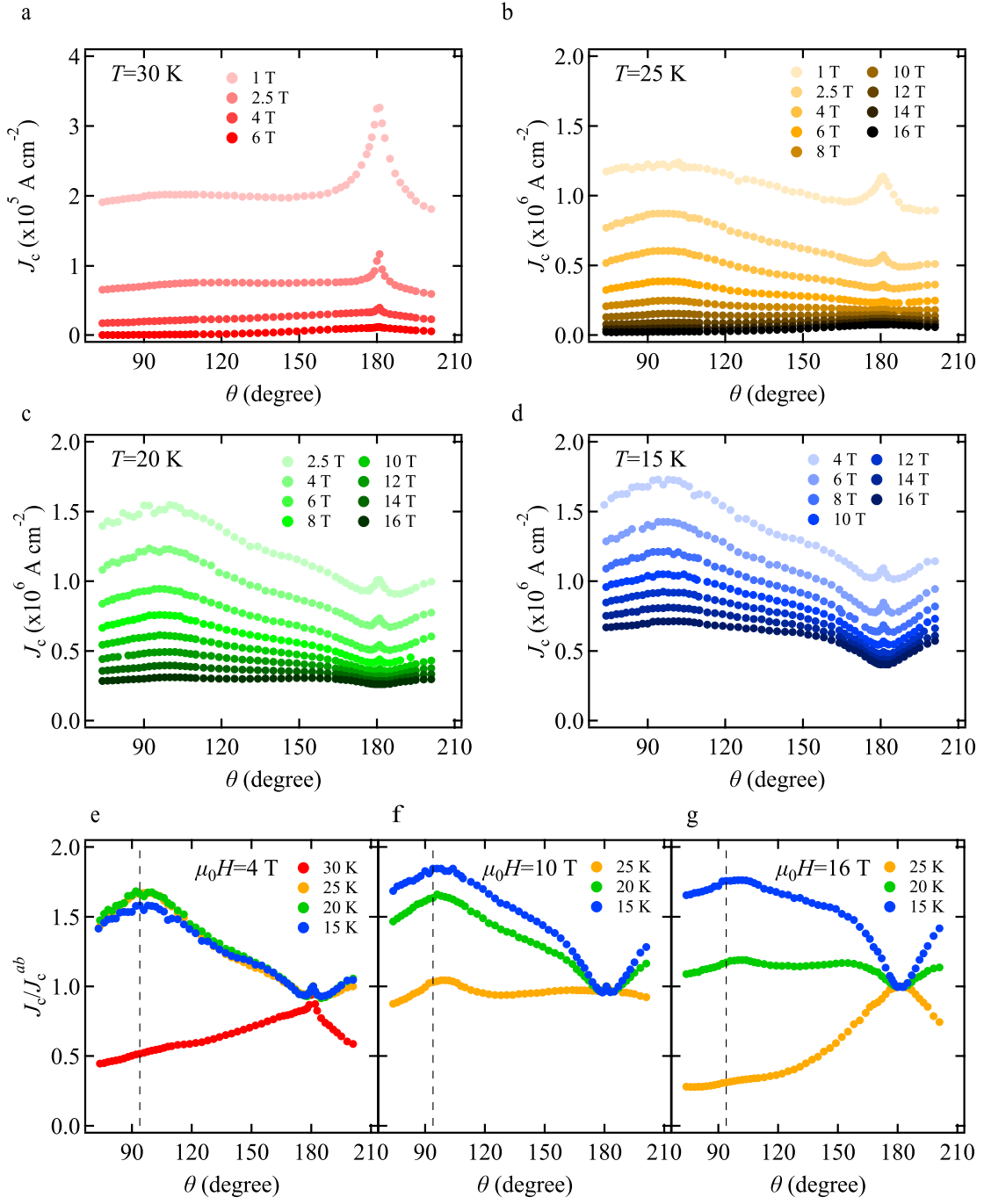
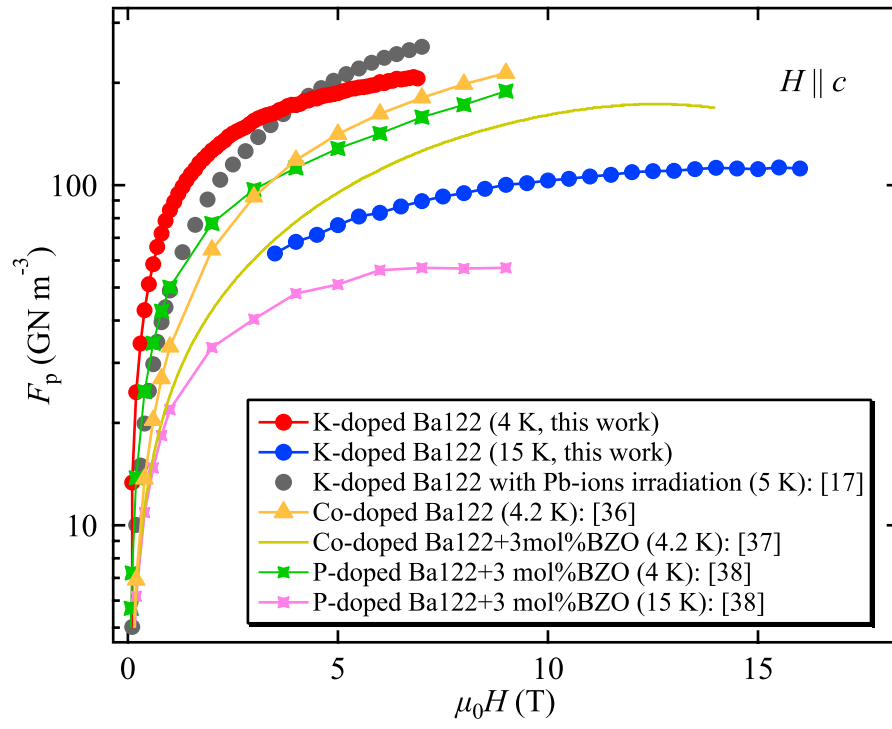


Figure 6



Supplementary information on “Approaching the ultimate superconducting properties of (Ba,K)Fe₂As₂ by naturally formed low-angle grain boundary networks”

Kazumasa Iida^{1,7}, Dongyi Qin², Chiara Tarantini³, Takafumi Hatano^{1,7}, Chao Wang⁴, Zimeng Guo⁵, Hongy Gao⁴, Hikaru Saito^{6,7}, Satoshi Hata^{4,5,7}, Michio Naito^{2,7}, Akiyasu Yamamoto^{2,7}

1 Department of Materials Physics, Nagoya University, Furo-cho, Nagoya 464-8603, Japan

2 Department of Applied Physics, Tokyo University of Agriculture and Technology, Koganei, Tokyo 184-8588, Japan

3 Applied Superconductivity Center, National High Magnetic Field Laboratory, Florida State University, Tallahassee, United States of America

4 The Ultramicroscopy Research Center, Kyushu University, 744 Motooka, Nishi, Fukuoka 819-0395, Japan

5 Interdisciplinary Graduate School of Engineering Sciences, Kyushu University, Kasuga, Fukuoka 816-8580, Japan

6 Institute for Materials Chemistry and Engineering, Kyushu University, Kasuga, Fukuoka 816-8580, Japan

7 JST CREST, Kawaguchi, Saitama 332-0012, Japan

1. Structural characterisation by X-ray diffraction

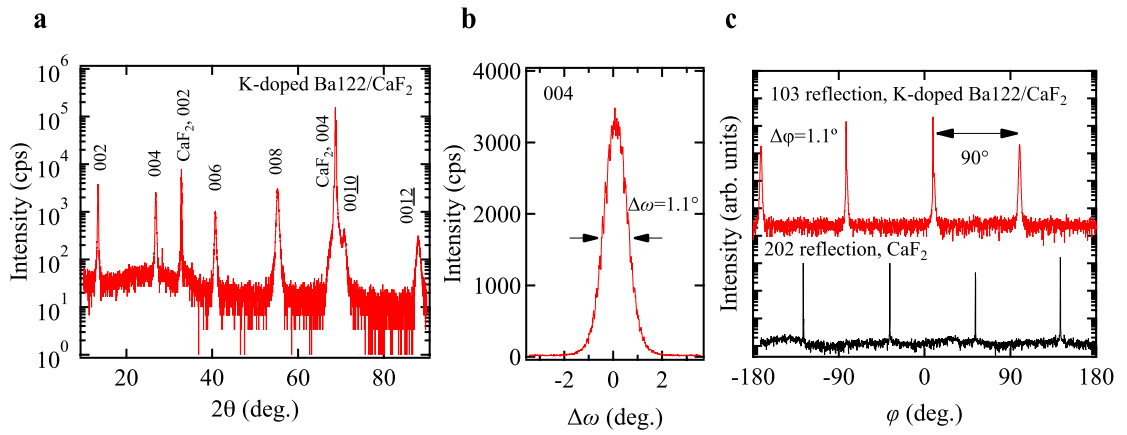


Figure S1 | Structural characterisation by X-ray diffraction (XRD) for the K-doped Ba122 thin film. a, $2\theta/\omega$ -scan. b, Rocking curve for the 004 reflection. c, Azimuthal ϕ -scan of the off-axis 103 reflection of K-doped Ba122 and 202 reflection of CaF₂. It is clear that phase-pure K-doped Ba122 is grown epitaxially on CaF₂. The epitaxial relation is identified as (001)[110]K-doped Ba122 || (001)[100]CaF₂.

2. The stereographic projection of K-doped Ba122 on the view direction of $[001]\text{CaF}_2$.

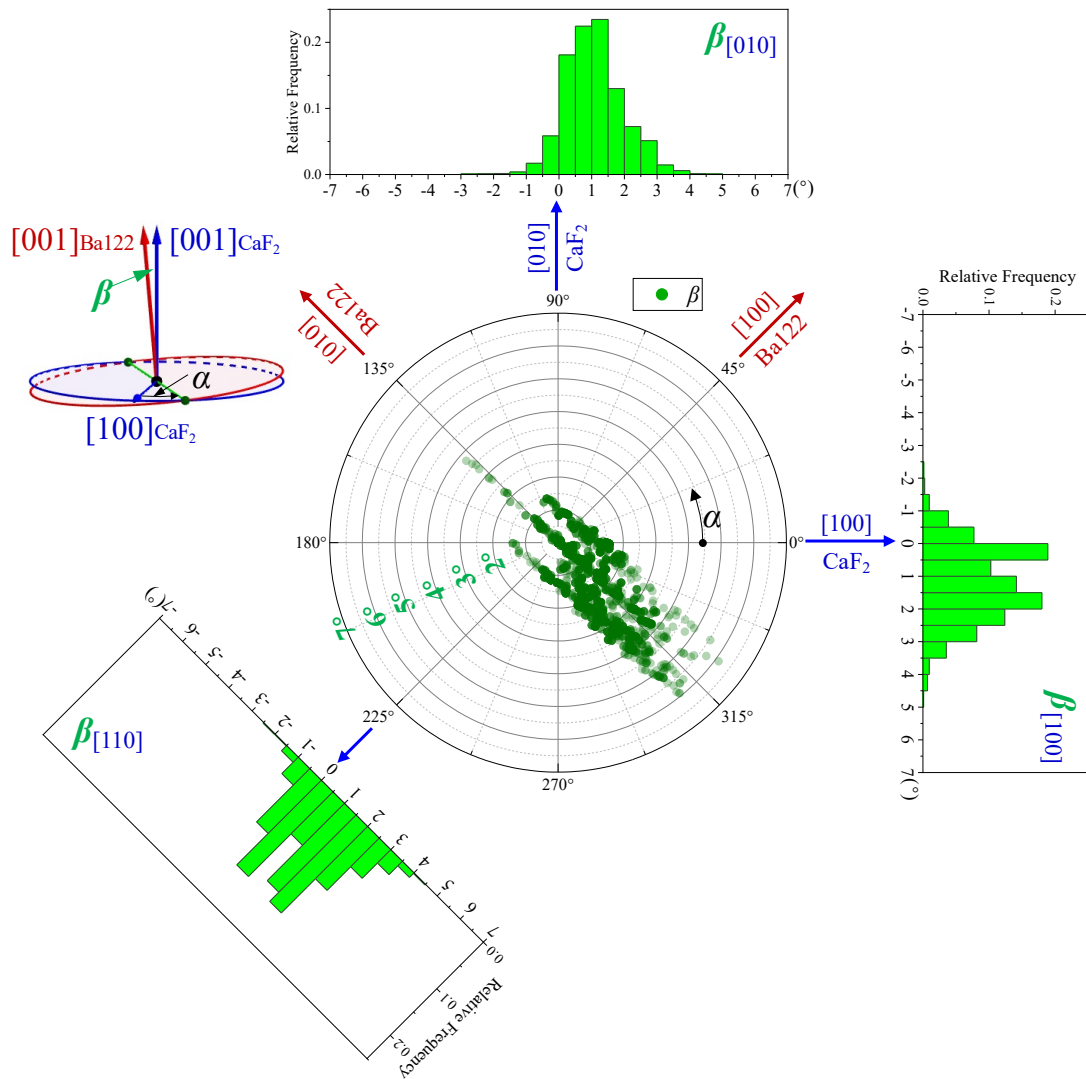


Figure S2 | The polar figure and the surrounding histograms of the out-of-plane misorientation of the K-doped Ba122 thin film. The histograms exhibit the distributions of β angle on three specific projected direction, $[100]\text{CaF}_2$, $[010]\text{CaF}_2$ and $[110]\text{CaF}_2$ (almost equivalent to the $[100]$ direction of K-doped Ba122). Euler angle α is defined as shown in the inset. As can be seen from this figure, the $[001]$ direction of K-doped Ba122 is tilted toward the $[0\bar{1}0]$ and its distribution (i.e. β) over the 2880 points shows that a large fraction locates between 0° – 3.5° and the peak position lies at around 1.5° .

3. In-plane misorientation angles of K-doped Ba122

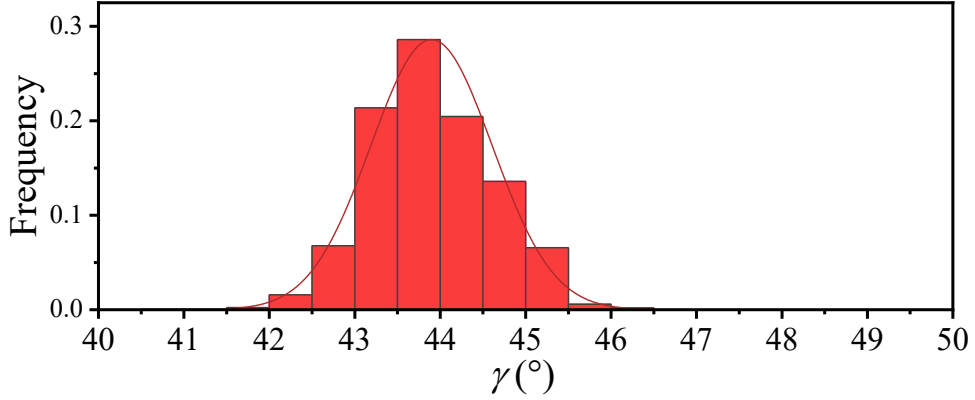


Figure S3 | The histogram of the in-plane misorientation of the K-doped Ba122 thin film. The distribution of γ shows that a large fraction lies 43°–45°.

4. Superconducting transition temperature T_c determined by resistive and magnetic measurements

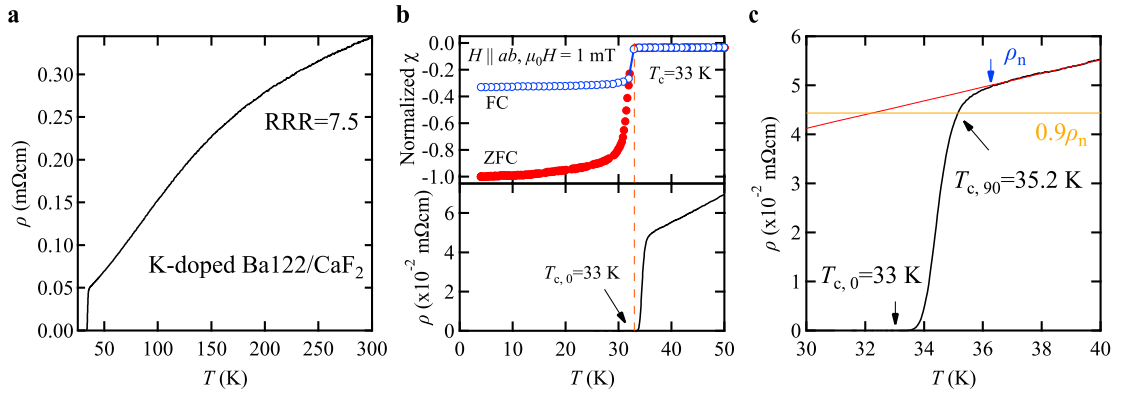


Figure S4 | Temperature dependence of the resistivity and magnetisation measurements for the K-doped Ba122 thin film. **a**, Resistivity curve $\rho(T)$ in the absence of magnetic field. Residual resistivity ratio (RRR), defined as $\rho(300\text{ K})/\rho_n$ (ρ_n : normal state resistivity, see below), is 7.5. Large RRR, low resistivity at 300 K and a sharp superconducting transition of 2.2 K ($T_{c,90} - T_{c,0}$, $T_{c,90}$: Temperature reaches 90% of ρ_n , $T_{c,0}$: Temperature reaches zero resistivity) compared to the polycrystalline films [S1] indicate that our K-doped Ba122 film is free of current-blocking impurities and with a good inter-grain connectivity. **b**, Temperature dependence of the normalised χ in the vicinity of the superconducting transition for field cooling (FC) and zero field cooling (ZFC) showed a T_c of 33 K. An external field of 1 mT was applied for $H \parallel ab$. This temperature coincides with $T_{c,0}$. **c**, Enlarged view of $\rho(T)$ in the vicinity of the transition. The blue arrow defines the normal state resistivity ρ_n below which the resistivity deviates from the linear fit to the normal state (red line).

5. E - J characteristics for evaluating J_c for various fields and temperatures

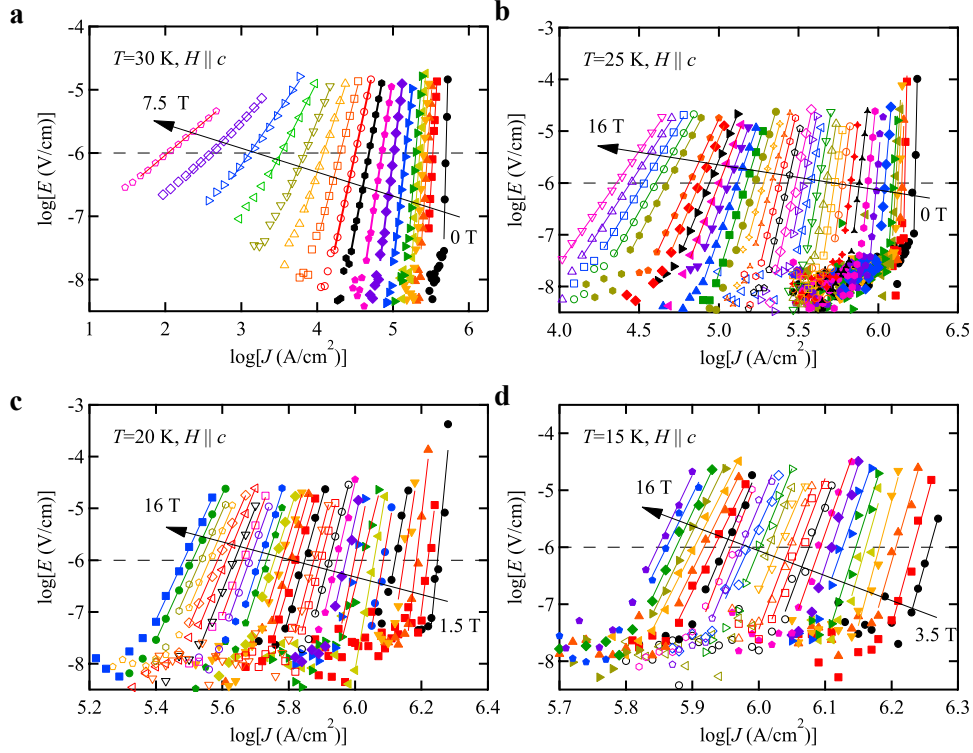


Figure S5 | Log-log plot of E - J characteristics for the K-doped Ba122 thin film. **a**, E - J curves measured for $H \parallel c$ at $T=30 \text{ K}$, **b**, 25 K, **c**, 20 K, and **d**, 15 K. The dashed line is the electric field criterion E_c for determining J_c . All curves show a power law behaviour, indicative of the absence of weak-link.

6. Magnetisation measurement to evaluate J_c

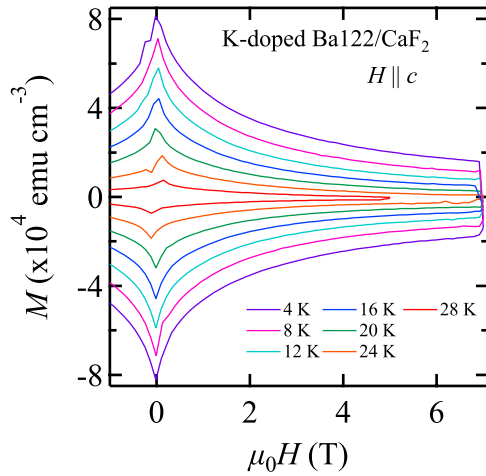


Figure S6 | Field dependence of magnetisation M . M - H hysteresis loops measured at various temperatures. Applied magnetic field is parallel to the c -axis.

Reference

S1 Lee, N., Jung, S-G., Kim, D. & Kang, W. Potassium-doped BaFe₂As₂ superconducting thin films with a transition temperature of 40 K. *Appl. Phys. Lett.* **96**, 202505 (2010).